**International Conference on Space Optics—ICSO 2012**
Ajaccio, Corse
9–12 October 2012

*Edited by Bruno Cugny, Errico Armandillo, and Nikos Karafolas*

# *Free-form reflective optics for mid-infrared camera and spectrometer on board SPICA*

*Naofumi Fujishiro*

*Hirokazu Kataza*

*Takehiko Wada*

*Yuji Ikeda*

*et al.*

International Conference on Space Optics — ICSO 2012, edited by Bruno Cugny, Errico Armandillo, Nikos Karafolas
Proc. of SPIE Vol. 10564, 105640G · © 2012 ESA and CNES · CCC code: 0277-786X/17/$18 · doi: 10.1117/12.2309046

# Free-form reflective optics for Mid-infrared Camera and Spectrometer on board SPICA

Naofumi Fujishiro*¶, Hirokazu Kataza†, Takehiko Wada†, Yuji Ikeda*‖, Itsuki Sakon‡ and Shinki Oyabu§
*Koyama Astronomical Observatory, Kyoto Sangyo University,
Motoyama, Kamigamo, Kita-ku, Kyoto, 603-8555, Japan
Email: naofuji@cc.kyoto-su.ac.jp
†Institute of Space and Astronautical Science, Japan Aerospace Exploration Agency,
3-1-1 Yoshinodai, Sagamihara, Kanagawa 229-8510, Japan
‡Department of Astronomy, School of Science, University of Tokyo,
7-3-1 Hongo, Bunkyo-ku, Tokyo 113-0033, Japan
§Department of Physics, Nagoya University, Furo-cho, Chikusa-ku, Nagoya, Aichi, 464-8601, Japan
¶Kyoto-Nijikoubou, 17-203 Iwakuraminami Osagi-cho, Sakyo-ku, Kyoto 603-0003, Japan
‖Photocoding, 61 Iwakurakita Ikeda-cho, Sakyo-ku, Kyoto 606-0004, Japan

***Abstract*—SPICA (Space Infrared Telescope for Cosmology and Astrophysics) is an astronomical mission optimized for mid- and far-infrared astronomy with a cryogenically cooled 3-m class telescope, envisioned for launch in early 2020s. Mid-infrared Camera and Spectrometer (MCS) is a focal plane instrument for SPICA with imaging and spectroscopic observing capabilities in the mid-infrared wavelength range of $5-38\mu$m. MCS consists of two relay optical modules and following four scientific optical modules of WFC (Wide Field Camera; $5' \times 5'$ field of view, $f/11.7$ and $f/4.2$ cameras), LRS (Low Resolution Spectrometer; $2'.5$ long slits, prism dispersers, $f/5.0$ and $f/1.7$ cameras, spectral resolving power $R \sim 50-100$), MRS (Mid Resolution Spectrometer; echelles, integral field units by image slicer, $f/3.3$ and $f/1.9$ cameras, $R \sim 1100-3000$) and HRS (High Resolution Spectrometer; immersed echelles, $f/6.0$ and $f/3.6$ cameras, $R \sim 20000-30000$). Here, we present optical design and expected optical performance of MCS. Most parts of MCS optics adopt off-axis reflective system for covering the wide wavelength range of $5-38\mu$m without chromatic aberration and minimizing problems due to changes in shapes and refractive indices of materials from room temperature to cryogenic temperature. In order to achieve the high specification requirements of wide field of view, small F-number and large spectral resolving power with compact size, we employed the paraxial and aberration analysis of off-axial optical systems (Araki 2005 [1]) which is a design method using free-form surfaces for compact reflective optics such as head mount displays. As a result, we have successfully designed compact reflective optics for MCS with as-built performance of diffraction-limited image resolution.**

## I. INTRODUCTION

SPICA (Space Infrared Telescope for Cosmology and Astrophysics) is an infrared astronomical mission led by the Japan Aerospace Exploration Agency (JAXA) in collaboration with the European Space Agency (ESA) and international consortiums in Japan, Europe, United States, the Republic of Korea and Taiwan [2]. In early 2020s, SPICA will be launched into a halo orbit around the second Lagrange point of the Sun-Earth system. The mission lifetime is 3 years (minimum) or 5 years (design). SPICA has a Ritchey-Chretien telescope composed of monolithic mirrors with 3.0m effective pupil diameter/3.2m physical diameter in the current design. The payload modules of SPICA are cooled down to less than 6K by multiple mechanical cryocoolers without a liquid Helium cryostat in order to reduce thermal background radiation emitted by itself. Cryogenic temperature will make SPICA more sensitive than passively cooled satellites of the James Webb Space Telescope and the Herschel Space Observatory in mid- and far-infrared region. Primary scientific goal of SPICA is understanding how galaxies, stars and planets form and evolve as well as the interaction between the astrophysical processes that have led to the formation of our own Solar System.

To achieve above scientific objectives, the Focal-Plane Instruments Assembly (FPIA) of SPICA is designed as shown in Fig. 1. FPIA consists of focal plane instruments (FPIs) and the Instrument Optical Bench (IOB). The FPIs for SPICA will be equipped to achieve significant progress for these main scientific objectives. Proposed instruments are a Mid-infrared Camera and Spectrometer (MCS), an imaging Fourier-transform spectrometer operating in far-infrared (SAFARI), a coronagraphic instrument (SCI) and focal plane cameras used for fine guidance (FPC). United States may provide another instrumentation.

MCS is a general purpose instrument for mid-infrared imaging and spectroscopy, covering the wavelength region of $5-38\mu$m with Si:As and Si:Sb detectors. We have been studying the MCS optics toward the SPICA international review which defines instruments and functions onboard. Taking account of the wide wavelength coverage of $5-38\mu$m, we adopt reflective optical system for the most part of MCS to minimize problems due to chromatic aberration as well as changes in physical properties of materials from ambient temperature to cryogenic temperature. Under rigid limitations of size and weight assigned to MCS in FPIA, high optical specifications, such as wide field of view, small F-number and large spectral resolving power, are required for scientific goals. In order to realize the specifications, we employed an optical design method proposed by Araki [1] for compact reflective

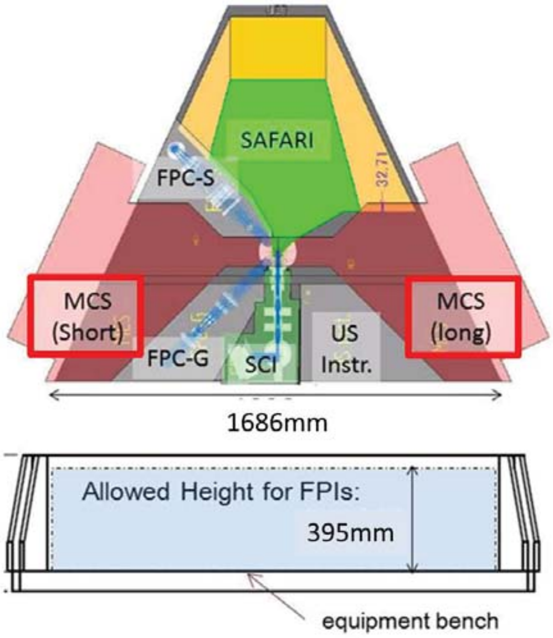

Fig. 1. The FPIA of SPICA. Red shaded regions indicate interspace assigned to MCS.

TABLE I
SPECIFICATIONS OF SCIENTIFIC OPTICAL MODULES OF MCS

| | WFC-S | WFC-L |
|---|---|---|
| Array format | Si:As (2K × 2K) | Si:Sb (1K × 1K) |
| Wavelength coverage | $5 - 25\mu$m | $20 - 38\mu$m |
| Filter bands | $5 - 25\mu$m, $R \sim 5$ | $20 - 38\mu$m, $R \sim 10$ |
| Pixel scale | 0".146/pixel | 0".293/pixel |
| FOV size | $5' \times 5'$ | $5' \times 5'$ |
| Image quality | Strehl ratio$>$ 0.8 | Strehl ratio$>$ 0.8 |
| | LRS-S | LRS-L |
| Array format | Si:As (2K × 2K) | Si:Sb (1K × 1K) or<br>Si:As high-dope (1K × 1K) |
| Wavelength coverage | $5 - 20\mu$m | $20 - 38\mu$m or<br>$25 - 48\mu$m |
| Pixel scale | 0".34/pixel | 0".73/pixel |
| Disperser | KBr prism | CsI prism |
| Spectral resolution | $R \sim 50 - 100$<br>$@\lambda = 10 - 25\mu$m | $R \sim 50 - 100$<br>$@\lambda = 20 - 38\mu$m |
| Slit length × width | $2'.5 \times 1".40$ | $2'.5 \times 2".66$ |
| | MRS-S | MRS-L |
| Array format | Si:As (2K × 2K) | Si:Sb (1K × 1K) |
| Wavelength coverage | $12.2 - 23.0\mu$m | $23.0 - 37.5\mu$m |
| Pixel scale | 0".40/pixel | 0".48/pixel |
| Disperser | echelle grating | echelle grating |
| Spectral resolution | $R \sim 1930$<br>$@\lambda = 22\mu$m | $R \sim 1060$<br>$@\lambda = 36\mu$m |
| Number of slice mirrors | 5 | 3 |
| Slice mirror length × width | 12" × 1".2 | 12" × 2".5 |
| | HRS-S | HRS-L |
| Array format | Si:As (2K × 2K) | Si:As (2K × 2K) |
| Wavelength coverage | $4 - 8\mu$m | $12 - 18\mu$m |
| Pixel scale | 0".288/pixel | 0".48/pixel |
| Disperser | ZnSe<br>immersion grating | CdTe or CdZnTe<br>immersion grating |
| Spectral resolution | $R \sim 30,000$ | $R \sim 20,000 - 30,000$ |
| Slit length × width | 3.5" × 0".72 | 6".0 × 1".2 |

optics.

In this paper, we firstly summarize the specifications of constituent optical modules of MCS. Secondly, we briefly describe the optical design method based on Araki's technique. Finally, we show optical layouts, expected optical performance and tolerance analysis of each optical module of MCS.

## II. MCS SPECIFICATIONS

Fig. 2 shows the structure of the MCS optics. MCS consists of 2 relay optics and 4 scientific optical modules. Table I summarize the specifications of the scientific modules. Field of view (FOV) and field definition assigned to each module is in Fig. 3. Each module of MCS has its own field in the telescope focal plane. Selection of module will be done by telescope pointing.

Short and Long Fore-optics are optics relayed to following scientific optical modules. Those two Fore-optics are mirror-image symmetric to each other with optically equivalent performance. Fore-optics compensates geometrical ray aberrations induced by the telescope and provides diffraction-limited images with the scientific optical modules. The telescope secondary is adopted as a pupil, and a filter wheel can be installed at an image conjugate of the pupil inside Fore-optics. Each scientific optical module has two channels (-S for short wavelength and -L for long wavelength) to cover wide wavelength ranges. WFC (Wide Field Camera) has two 5 arcminutes square FOVs. WFC-S covers the wavelength range from 5 to 25 micron and WFC-L covers the wavelength range from 20 to 38 micron. LRS (Low Resolution Spectrometer) adopts prism dispersers and covers the wavelength range from 5 to 38 micron (optional: 5 to 48 micron) with spectral resolving power, $R$, of $50 - 100$. It also has two channels, LRS-S and LRS-L. These channels share the same FOV by means of a dichroic beam splitter. MRS (Mid Resolution Spectrometer) has integral field units by image slicer and echelle gratings with cross-disperser gratings[3]. It covers the wavelength range from 12.2 to 23.0 micron with $R \sim 1000$ by MRS-S and the wavelength range from 23.0 to 37.5 micron with $R \sim 2000$ by MRS-L. HRS (High Resolution Spectrometer) covers the wavelength range from 12 to 18 micron with $R \sim 20000 - 30000$ (HRS-L), and we also have studied optional short wavelength channel which covers the wavelength range from 4 to 8 micron with $R \sim 30000$ (HRS-S). HRS realizes high spectral resolution using immersed echelle gratings and refractive optics.

All optical modules except for HRS adopt reflective optical system. It is beyond the scope of this paper to argue the refractive optics of HRS in detail. For further description of HRS, see Kataza[4].

## III. OPTICAL DESIGN METHOD

We have carried out the design of the MCS reflective optics using the aberration analysis proposed by Araki and an automatic design technique based on the method of damped least square with a commercial ray-tracing software.

In conventional design of reflective optics, with the idea

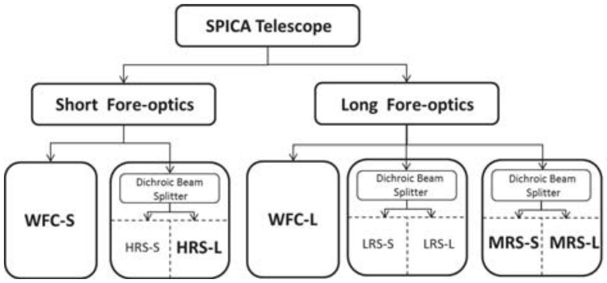

Fig. 2. Structure of MCS. Bold fonts indicate optical modules identified as mandatory or high rated option in the mid term report of the SPICA international review.

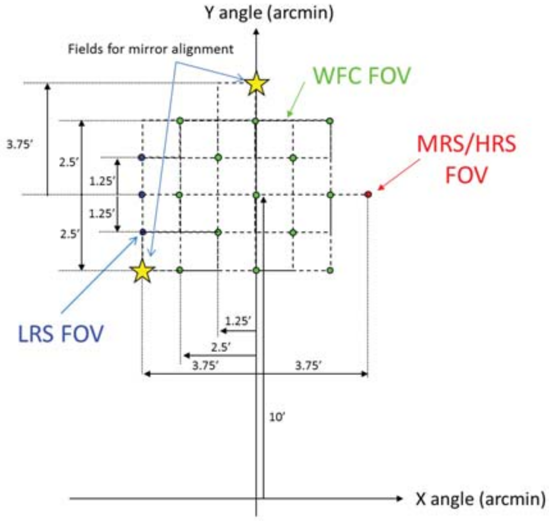

Fig. 3. FOV and field definition of MCS. Large stars (yellow) show fields used for mirror alignment of Fore-optics in laboratory testing.

of so-called ”de-centered optical systems”, we often face the problem that we cannot optimize the optical systems with a fixed optical framework. Araki redefined ”off-axial optical systems” as an extended concept of co-axial optical systems, where deflection surfaces are arranged along the folded reference axes. Fig. 4 shows the concept of the off-axial optical systems. In the off-axial optical systems, a reference ray, originating from an object plane on an optical axis and traveling along the optical axis, strikes vertexes of all subsequent reflection surfaces. As a matter of course, a reflection angle of the reference ray against a surface normal at a vertex equals a corresponding incident angle. As shown in Fig.4, z-directions of local reference axes are parallel to surface normals at the reflection surfaces or traveling directions of the reference ray between the reflection surfaces. In the aberration analysis for the off-axial optical systems, each constituent surface is expressed in the following equation on a local coordinate:

$$
\begin{aligned}
z(x,y) &= C_{20}x^2 + C_{11}xy + C_{02}y^2 \\
&+ \quad D_{30}x^3 + D_{21}x^2y + D_{12}xy^2 + D_{03}y^3 \\
&+ \quad E_{40}x^4 + E_{31}x^3y + E_{22}x^2y^2 + E_{13}xy^3 + E_{04}xy^4 \\
&+ \quad \cdots . \qquad (1)
\end{aligned}
$$

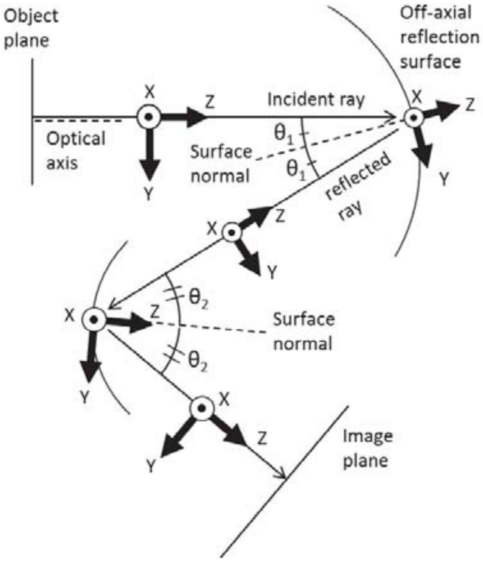

Fig. 4. Concept of the off-axial optical system.

Using this expression, we can optimize the surface configuration without changing the framework of the reference axes. Since mirrors can be placed freely as designer’s intent, it is suitable for design of compact reflective optics such as head mount displays.

Here is the outline of the design method.

1) Design an optical power distribution of an optical system with desired focal length using conventional paraxial analysis for co-axial optical system.
2) Arrange flat mirrors in the optical system with consideration of surface interference and interspace limitation. Each flat mirror corresponds with a optical power determined above. A separation distance between the flat mirrors is fixed with a distance between corresponding optical powers in the paraxial design.
3) Add optical powers to the flat mirrors without azimuthal dependence of paraxial quantities by the following formulas:

$$
\begin{aligned}
C_{20} &= \frac{\Phi}{4\cos\theta}, \qquad (2) \\
C_{02} &= \frac{\Phi\cos\theta}{4}, \qquad (3)
\end{aligned}
$$

where $\Phi$ is the optical power assigned to the mirror and $\theta$ is the incident angle of the reference ray against the surface normal of the mirror.
4) Optimize higher order terms of the free-form surfaces using the automatic design of the software under required constraints to achieve specifications.
5) Confirm as-built optical performance by tolerance analysis based on the Monte Carlo method.

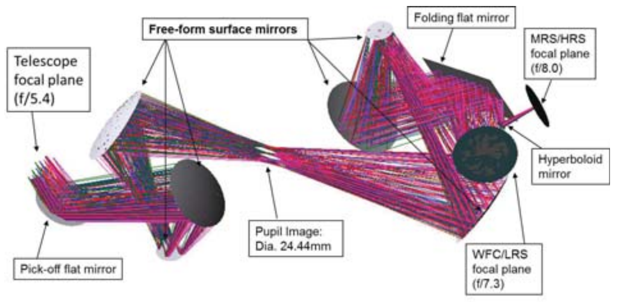

Fig. 5. Bird's view of the Fore-optics optical layout.

## IV. RESULTS

### A. *Optical Layouts*

Fig. 5 shows a bird's view of the Short Fore-optics layout. Long Fore-optics and Short Fore-optics are mirror-image symmetrical with respect to a plane including the optical axis of the telescope. The optics consists of 6 free-form surface mirrors, a pick-off flat mirror, a folding flat mirror and a hyperboloid mirror. We adopted the optical power distribution of Three-Mirror Korsch Objective [5] to achieve wide FOV and moderately fast F-number. In order to use optical filters of $\phi$30mm, the pupil image diameter was reduced to $\phi$24.44mm. At the position of the intermediate pupil image, we can install a disk-shaped filter wheel of $\phi$260mm$\times$50mm. During optimization process, there is a trade-off between the size and the wavefront error of the pupil image. We assigned high priority to minimization of the pupil image size. Consequently, the wavefront errors at the pupil image position are larger than a wavelength unit at wavelength, $\lambda$, of 5 micron. The hyperboloid mirror is located after the folding flat mirror to pick up beams and make F-number slower for MRS or HRS. The effective F-numbers of Fore-optics are $f/7.3$ (WFC/LRS) and $f/8.0$ (MRS/LRS).

Fig.6 shows a top view of the combination of Short Fore-optics and WFC-S. $f/7.3$ output beams of Short Fore-optics deflect off the final folding mirror into the compartment of WFC-S. The angle between reference axes of Short Fore-optics and WFC-S on the top view is 115 degrees. Fig.7 shows a side view of WFC-S only. WFC-S consists of 5 free-form surface mirrors and a folding flat mirror. Like Fore-optics, the size of the intermediate pupil image inside WFC-S was reduced to $\phi$24.26mm for the use of $\phi$30mm optical filters with a $\phi$260mm$\times$50mm filter wheel. The effective F-number of WFC-S is $f/11.7$ which realizes 5'x5' FOV and Nyquist sampling of diffraction-limited images at $\lambda = 5\mu$m on the 2K$\times$2K Si:As detector with pixel size of 25$\mu$m.

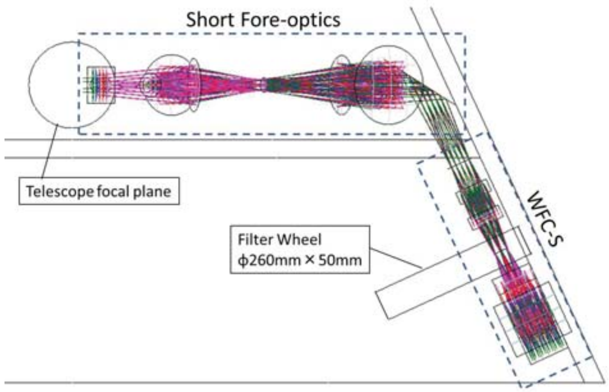

Fig. 6. Top view of the WFC-S optical layout including Short Fore-optics.

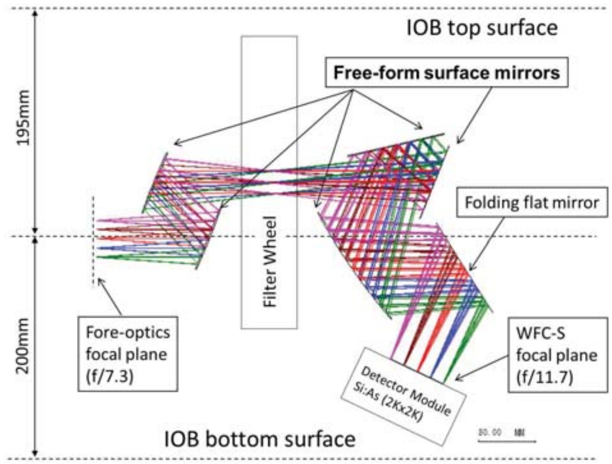

Fig. 7. Side view of the WFC-S optical layout.

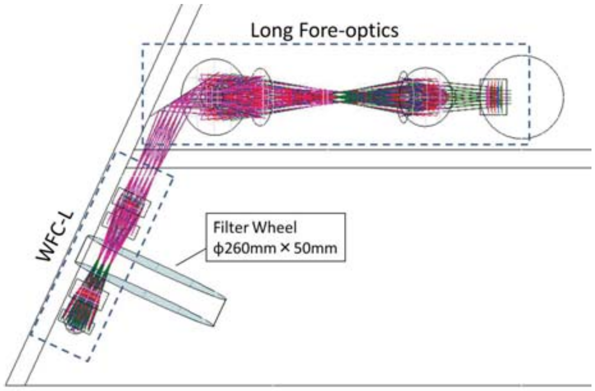

Fig. 8. Top view of the WFC-L optical layout including Long Fore-optics

Fig.8 shows a top view of the combination of Long Fore-optics and WFC-L. The angle between reference axes of Long Fore-optics and WFC-L on the top view is 115 degrees. Fig.9 shows a side view of WFC-L only. WFC-L consists of 6 free-form surface mirrors. Like Fore-optics and WFC-S, the size of the intermediate pupil image inside WFC-L was reduced to $\phi$23.90mm for the use of $\phi$30mm optical filters with $\phi$260mm$\times$50mm filter wheel. The effective F-number of WFC-L is $f/4.2$ which matches 5'x5' FOV. Nyquist sampling of diffraction-limited images is achieved at $\lambda > 7\mu$m on the 1K$\times$1K Si:Sb detector with pixel size of 18$\mu$m..

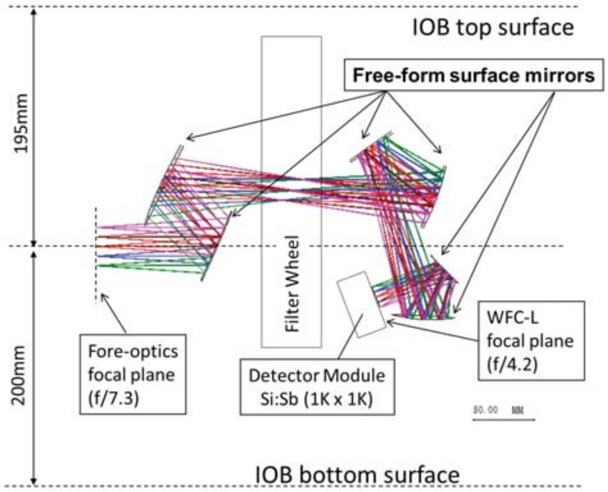

Fig. 9. Side view of the WFC-L optical layout.

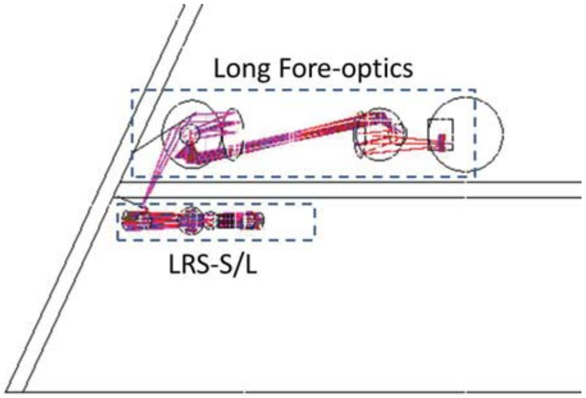

Fig. 10. Top view of the LRS optical layout including Long Fore-optics

Fig.10 shows a top view of the combination of Long Fore-optics and LRS. The final folding mirror of Fore-optics reflects $f/7.3$ output beams into the compartment of LRS. Fig. 11 shows a side view of LRS only. LRS consists of 15 free-form surface mirrors, 4 folding flat mirrors and 2 dispersion prisms. The LRS optical bench is in the back of the optical bench of Long Fore-optics. The first 3 folding flat mirrors after the focal plane of Long Fore-optics make dispersion direction of prisms parallel to the plane of the optical bench. The dichroic beam splitter after the first collimator optics reflects $\lambda < 20\mu$m beams into LRS-S and refracts $\lambda > 20\mu$m beams into LRS-L. 2.5 'slits are installed at re-imaging planes formed by the first camera optics for both LRS-S and LRS-L. After the second collimators, a KBr prism with apex angle of 62deg and a CsI prism with apex angle of 58deg are installed for LRS-S and LRS-L respectively. Finally, $f/5.0$ and $f/1.7$ camera optics make Nyquist sampling of diffraction-limited images at $\lambda = 10\mu$m on the 2K×2K detector of LRS-S and at $\lambda = 20\mu$m on the 1K×1K detector of LRS-L respectively.

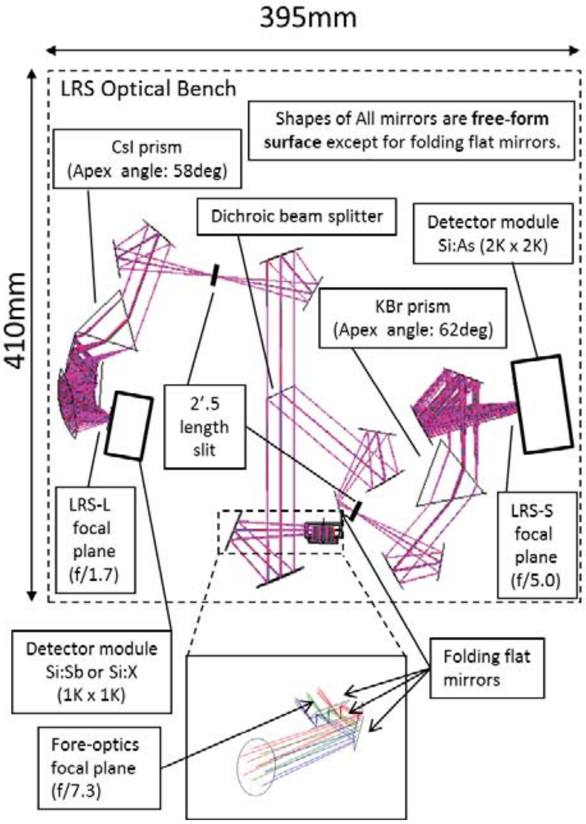

Fig. 11. Side view of the LRS optical layout.

Fig. 12 shows a top view of the combination of Long Fore-optics and MRS. The hyperboloid mirror of Long Fore-optics reflects $f/8.0$ output beams into the compartment of MRS. Fig. 11 shows a side view of MRS only. MRS consists of 16 free-form surface mirrors, 2 folding flat mirrors, 2 integral field units, 2 cross-dispersion gratings and 2 echelle gratings. The optical bench of MRS are placed on the outside wall of IOB. After the focal plane of Long Fore-optics, 2 free-form mirrors and a folding flat mirror make collimated beams traveling parallel to the optical bench. The dichroic beam splitter reflects $\lambda < 23\mu$m beams into MRS-S and refracts $\lambda > 23\mu$m beams into MRS-L. The integral field units (IFUs) follow the first camera optics for both MRS-S and MRS-L. The optics of both MRS-S and MRS-L IFUs was based on the idea of the advanced image slicer proposed by Content [6]. Fig.14 shows a bird's view of the MRS-L IFU for instance. The IFUs place multiple reflective slits at the refocus position of the first camera optics. The multiple slits are placed almost in parallel but slightly tilted to each other. Then, light rays reflected at the different slits travel into different directions, where different camera optics of spherical mirror are placed, and re-imaged on a pseudo slit position being arranged to be laid in a line. Multiple tilted mirrors are placed on the pseudo slit position to improve telecentricity for design of following spectrometers. Folding flat mirrors and the second collimator optics follow

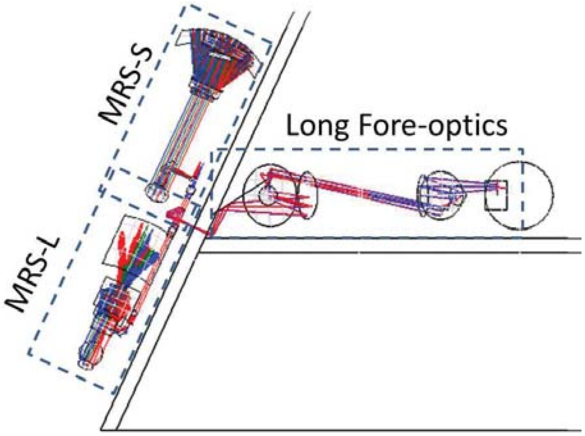

Fig. 12. Top view of the MRS optical layout.

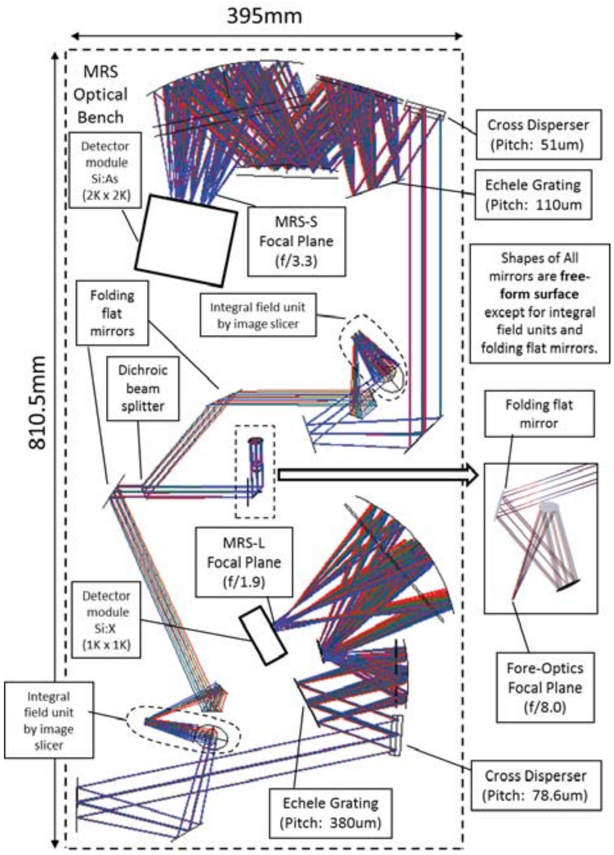

Fig. 13. Side view of the MRS optical layout.

IFUs. Cross-dispersion gratings with pitch of $51\mu$m (MRS-S) and $78.6\mu$m (MRS-L) and echelle gratings with pitch of $110\mu$m (MRS-S) and $380\mu$m (MRS-L) are placed near the pupil image made by the second collimator optics. Finally, $f/3.3$ and $f/1.9$ camera optics form echellograms of pseudo slit images on the 2K×2K detector of MRS-S and the 1K×1K detector of MRS-L respectively.

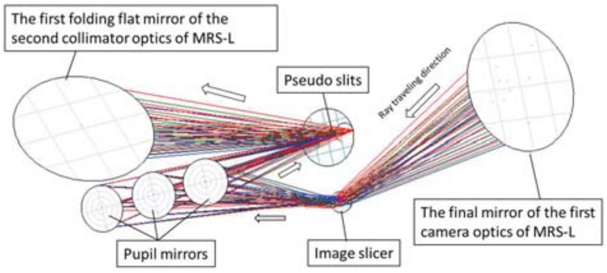

Fig. 14. Bird's view of the integral field unit of MRS-L.

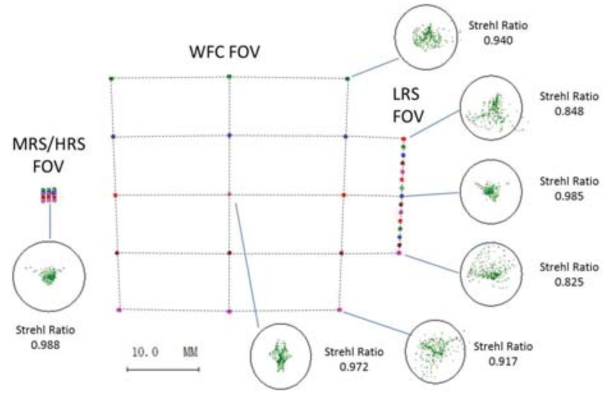

Fig. 15. Footprint diagrams and spot diagrams at fore-optics focal plane. Circles indicate Airy disks at $\lambda = 5\mu$m.

## *B. Expected Optical Performance*

Fig. 15 shows footprint diagrams and spot diagrams of some representative field images on the focal plane of Fore-Optics. Strehl ratios of all field images at $\lambda = 5\mu$m are larger than 0.825. The maximum distortion expressed as a percentage of the paraxial image height at the WFC / LRS focal plane is $4.7\%$. It does not have a significant impact on the subsequent optical system. In the calculation of the Strehl ratio, we did not take a diffraction effect by obscuration of a baffle of the telescope secondary mirror into consideration.

Fig. 16 shows footprint diagrams and spot diagrams of some representative field images on the focal planes of WFC-S and WFC-L. Strehl ratios of all field images at $\lambda = 5\mu$m are larger than 0.872 for both WFC-S and WFC-L. The maximum distortions the focal planes are $5.45\%$ and $5.79\%$ for WFC-S and WFC-L respectively. We can correct the image distortions in data reduction processes. Although operating wavelength of WFC-L is larger than $20\mu$m, we have designed the WFC-L optics to achieve diffraction-limited image resolution at $\lambda = 5\mu$m for a back-up use from WFC-S.

Fig. 17 shows footprint diagrams and spot diagrams of some representative field images on the focal planes of LRS-S and LRS-L. Because there is a trade-off between image quality and distortion, we set high priority on the imaging performance. Thus, the distortions are relatively large, but we can correct the distortions in data reduction processes. Strehl ratios of all images field of LRS-S at $\lambda > 10\mu$m, which realizes Nyquist

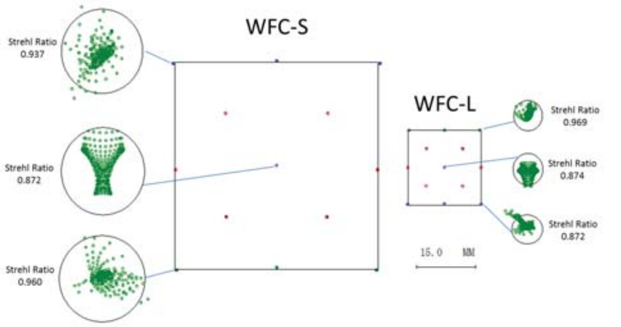

Fig. 16. Footprint diagrams and spot diagrams at WFC-S/L focal planes. Circles indicate Airy disks at $\lambda = 5\mu$m.

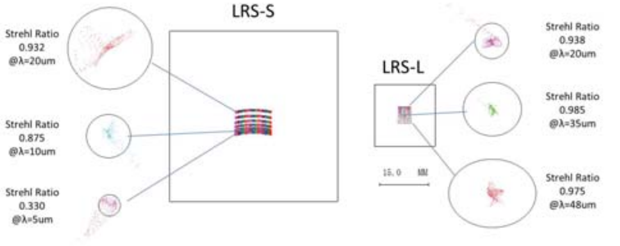

Fig. 17. Footprint diagrams and spot diagrams at LRS-S/L focal planes. Circles indicate Airy disks.

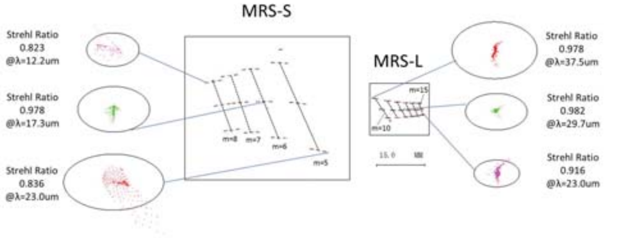

Fig. 18. Echellograms and spot diagrams at MRS-S/L focal planes. Circles indicate Airy disks.

sampling, are larger than 0.875. At $\lambda < 10\mu$m, the LRS-S detector is in undersampling condition, i.e. the pixel size of the detector determines its spectral resolution. Strehl ratios of all field images of LRS-L at all wavelength are larger than 0.938. Fig. 19 shows spectral resolving power, $R$, of both LRS-S and LRS-L, which mostly satisfies the goal value of R = 50-100.

Fig. 18 shows echellograms and spot diagrams of some representative field images on the focal planes of MRS-S and MRS-L. Strehl ratios of MRS-S images at $\lambda = 12 - 23\mu$m and all diffraction orders of $m = 5 - 8$ are lareger than 0.823. Strehl ratios of MRS-L images at $\lambda = 23 - 37\mu$m and all diffraction orders of $m = 10 - 15$ are lareger than 0.916. Fig. 19 shows spectral resolving power, $R$, of both MRS-S and MRS-L, which satisfies the specification values.

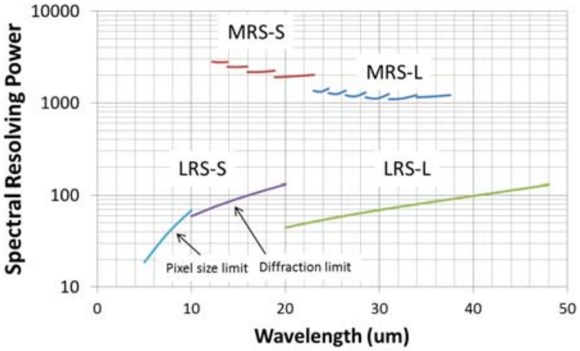

Fig. 19. Spectral resolving power, R, of LRS and MRS for point sources.

### C. Tolerance Analysis

We have evaluated as-built image performance with consideration of assembling errors by the tolerance analysis based on the Monte Carlo method. As shown in Fig. 20, we defined shift decenters in $X, Y, Z$ and tilt decenters in $\alpha, \beta, \gamma$ for all mirrors and sub-optical benches. We assigned tolerances of $\pm 0.05$mm or more to shift decenters and tolerances of $\pm 0.001$radians or more to tilt decenters. We applied uniform probability distributions to the tolerances. For LRS and MRS, we assumed that constituent sub-optics of pre-optics with dichroic beam splitter, IFUs and spectrometers are assembled on corresponding sub-optical benches, which allows us to perform laboratory testing of each sub-optics separately.

As shown in the left panel of Fig. 21, we assumed that the SPICA telescope or a telescope simulator provides incident lights with Fore-optics, i.e. we took ray aberration introduced by the telescope into account. We defined the tilt decenters of $\alpha$ and $\beta$ at the fourth free-form surface mirror of Fore-optics as compensators in the tolerance analysis. We assumed that geometrical spots of the field images for the mirror alignment defined in Fig. 3 can be evaluated in visible wavelength by small CCD detectors installed at the Fore-optics focal plane. Firstly, we generated 1000 optical models with random displacements on the probability distribution to the decenters of mirrors and sub-optical benches. Secondly, for each model with random perturbation, we minimized RMS spot diameters of the field images for mirror alignment by changing $\alpha$ and $\beta$ angles of the fourth free-form mirror. Finally, we evaluated Strehl ratios of the field images of scientific FOVs at $\lambda = 5\mu$m for 1000 models and calculate their cumulative probabilities. The right panel of Fig. 21 shows the cumulative probability distribution of Strehl ratio for Short Fore-optics. As previously explained, since Long Fore-optics is mirror-image symmetric to Short Fore-optics, Long Fore-optics has the same cumulative probability as Short Fore-optics. Diffraction-limited performance with Strehl ratio of more than 0.8 will be achieved more than $20\%$ of the time for all field images of scientific FOVs. According to the result, it is not difficult to realize actual Fore-optics with diffraction-limited image resolution if we carefully designed opto-mechanics and built

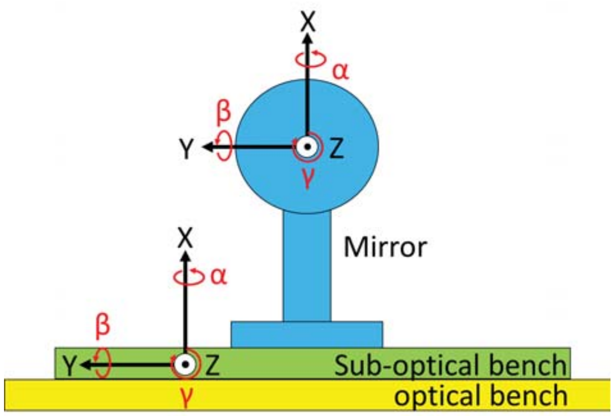

Fig. 20. Definition of decentering coordinates for mirrors and sub-optical benches.

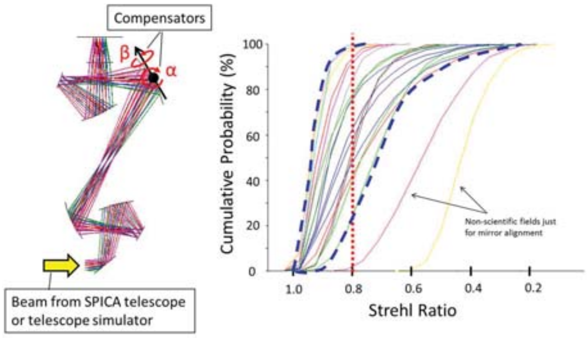

Fig. 21. Left: Conditions of the tolerance analysis for Short Fore-optics. Right: Cumulative probability of Strehl ratio for Fore-optics at $\lambda = 5\mu$m. Solid curves indicate each image field of scientific FOV. Dashed curves (blue) indicate maximum/minimum values of the cumulative probability at a given Strehl ratio. Vertical dotted line lies on strehl ratio of 0.8.

the optics.

Next, we generated 500 perturbed models of WFC-S and WFC-L with the random displacements. We connected them to random perturbed models of Short and Long Fore-optics respectively after optimization of the tilt of the fourth free-form mirror. Then, we evaluated Strehl ratios of the field images at the focal planes of WFC-S and WFC-L at $\lambda = 5\mu$m for the 500 combined models and calculate their cumulative probabilities. Fig.22 shows the cumulative probability distributions of Strehl ratio for WFC-S and WFC-L. Like Fore-optics, diffraction-limited performance with Strehl ratio of more than 0.8 will be achieved more than around 20% of the time for all field images. It probably has no issue with actual optics of WFC-S and WFC-L if we carefully developed them.

We performed tolerance analyses for LRS and MRS in the same way as WFC. Fig. 23 and 24 show to the cumulative probability distributions of Strehl ratio for LRS and MRS respectively. LRS-S is expected to achieve diffraction-limited performance more than 20% of the time at $\lambda = 10 - 20\mu$m. At $\lambda < 10\mu$m, LRS-S has undersampled images with $25\mu$m pixel size and its spectral resolving power is determined by the pixel size. LRS-L, MRS-S and MRS-L can easily achieve diffraction-limited image resolution over their whole wavelength range.

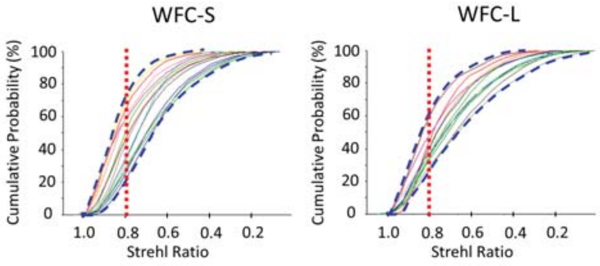

Fig. 22. Cumulative probability of Strehl ratio for WFC at $\lambda = 5\mu$m.

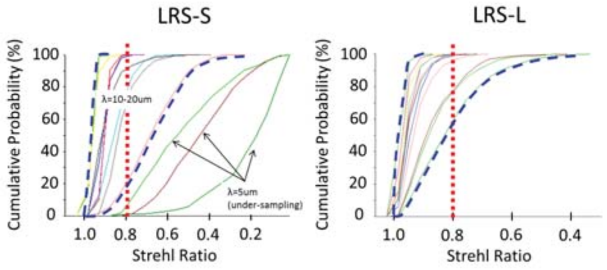

Fig. 23. Cumulative probability of Strehl ratio for LRS.

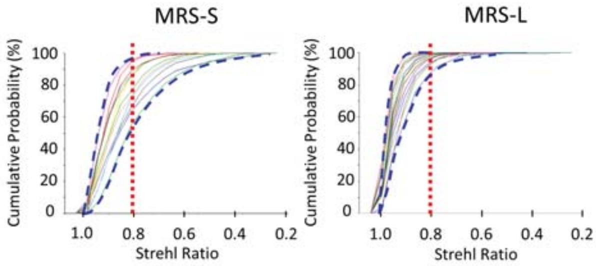

Fig. 24. Cumulative probability of Strehl ratio for MRS.

## V. CONCLUSION

We have designed 2 relay optical modules of Short and Long Fore-optics, the wide field cameras of WFC, the low-resolution spectrometer of LRS and the mid-resolution spectrometer of MRS using free-form surface mirrors for the mid-infrared instrument of MCS onboard SPICA. We adopted the optical design method proposed by Araki which allow us to construct optical frameworks freely and apply conventional paraxial analysis to determination of optical power distribution. We have succeeded in deriving optimal solutions to achieve the high scientific requirements, such as bright F-number, wide FOV and high spectral resolution with compact size. We also have carried out the tolerance analysis based on the Monte Carlo method and demonstrated as-built performance of diffraction-limited image resolution with just 2 compensators assigned to the fourth free-form surface mirror of Fore-optics.

## REFERENCES

[1] Araki,K., ”Paraxial and aberration Analysis of off-axial optical systems”, 12, 3,221, Opt. Rev. (2005).

[2] Nakagawa, T., Matsuhara, H. and Kawakatsu, Y., ”The next-generation infrared astronomy mission SPICA”, 8442, Proc. SPIE (2012).

[3] Sakon, I., Kataza, H., Onaka, T., Ikeda, Y., Fujishiro, N., Mitsui, K. and Okada, N., ”Recent progress in the development of mid-infrared medium resolution spectrometer (MRS) installed in SPICA/MCS”, 8442, Proc.SPIE (2012).

[4] Kataza, H., Wada, T., Sakon, I., Kobayashi, N., Sarugaku, Y., Fujishiro, N., Ikeda, Y. and Oyabu, S., ”Mid-infrared Camera and Spectrometer on board SPICA”, Proc.SPIE (2012).

[5] Bass, M., DeCusatis, C., Li, G., Mahajan, V.N. and Stryland, E.V., *Handbook of Optics, Vol. I: Geometrical and Physical Optics, Polarized Light, Components and Instruments*, 3rd Edition, McGraw-Hill, New York. (2010).

[6] Content,R., hAdvanced Image Slicers for Integral Field Spectroscopy with UKIRT and GEMINIh, Proc. SPIE 3354, 187-200 (1998).